Journal of Power Sources 628 (2025) 235891

Contents lists available at ScienceDirect

Journal of Power Sources

journal homepage: www.elsevier.com/locate/jpowsour

Uncovering the battery direct current internal resistance puzzle: A machine learning-driven pore network approach

Meiyuan Jiao [a,1], Pan Huang [a,d,1], Zheyuan Pang [a], Sijing Wang [a], Honglai Liu [a,b], Yiting Lin [a,c,**], Cheng Lian [a,b,*]

[a] State Key Laboratory of Chemical Engineering, Shanghai Engineering Research Center of Hierarchical Nanomaterials, School of Chemical Engineering, East China University of Science and Technology, Shanghai 200237, China
[b] School of Chemistry and Molecular Engineering, East China University of Science and Technology, Shanghai 200237, China
[c] School of Mechanical and Power Engineering, East China University of Science and Technology, Shanghai 200237, China
[d] Product Planning and New Auto Technologies Research Institute, BYD Auto Industry Company Limited, Shenzhen 518118, China

HIGHLIGHTS

- A machine learning-driven pore network approach is proposed.
- Thickness, porosity, and average particle size significantly affect DCIR.
- The equation relating DCIR to electrode structure is clarified.

GRAPHICAL ABSTRACT

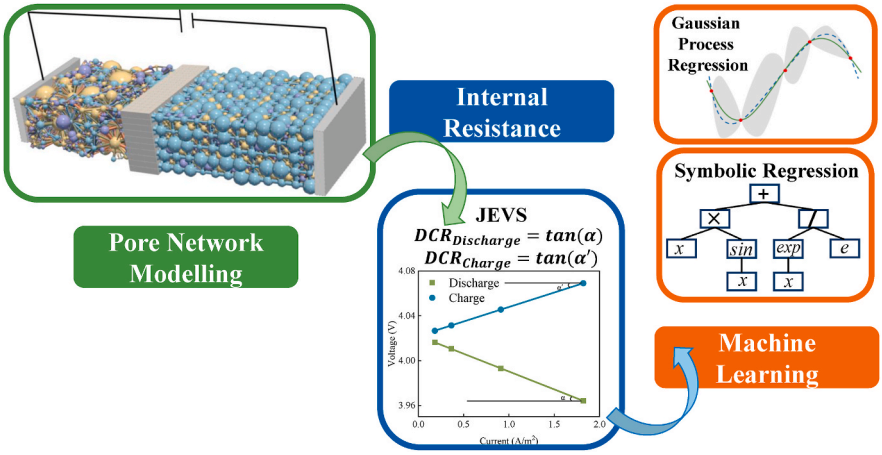

ARTICLE INFO

Keywords:
Pore network model
Structure-activity relationships
Machine learning
Direct current internal resistance

ABSTRACT

Direct current internal resistance (DCIR), as a fundamental characteristic of lithium-ion batteries, serves as a critical indicator for the accurate estimation and prediction of battery health. The DCIR of a battery is affected by the electrode structure. Despite its significance, the relationship between the electrode structure and the DCIR during charging and discharging remains unclear. Based on a pore network model of a lithium manganate cell, this work focuses on the cathode and quantifies the effects of cathode thickness (L), porosity (ε), connectivity (G),

* Corresponding author. State Key Laboratory of Chemical Engineering, Shanghai Engineering Research Center of Hierarchical Nanomaterials, School of Chemical Engineering, East China University of Science and Technology, Shanghai 200237, China.
** Corresponding author. State Key Laboratory of Chemical Engineering, Shanghai Engineering Research Center of Hierarchical Nanomaterials, School of Chemical Engineering, East China University of Science and Technology, Shanghai 200237, China.
E-mail addresses: linyiting@ecust.edu.cn (Y. Lin), liancheng@ecust.edu.cn (C. Lian).
[1] Equally contributing authors.

https://doi.org/10.1016/j.jpowsour.2024.235891
Received 26 September 2024; Received in revised form 9 November 2024; Accepted 17 November 2024
Available online 23 November 2024

average particle size (d) and specific surface area (S/V) on DCIR. Combined with machine learning, this work identify that cathode thickness, porosity and average particle size the primary determinants of the DCIR, and the formulas for calculating charging and discharging DCIR are derived, $DCIR_{Charge} = 0.168Ld^4/\varepsilon^{2.5}$ and $DCIR_{Discharge} = 0.072Ld^3/\varepsilon^2$. This work proposes a research framework for predicting DCIR from the electrode structure, which is applicable to most porous electrode batteries, providing a theoretical basis for calculating the DCIR and is of great significance for electrode design.

1. Introduction

Lithium-ion batteries (LIBs), as the preferred energy storage devices for portable electronic devices and electric vehicles [1], have received much attention for their charging capabilities [2–4], thermal safety [5–7] and batteries state of health [8,9], which are closely related to the internal resistance of the batteries. Battery internal resistance consists of ohmic internal resistance, concentration polarization internal resistance and electrochemical polarization internal resistance [10–12].Battery resistance estimation techniques mainly include direct current (DC) methods and alternating current (AC) methods [13], of which the DC method is commonly used because of its simplicity and its ability to accurately reflect the ohmic and polarized internal resistance [14]. Complex porous electrodes affect the transport of ions and electrons as well as the electrochemical reactions inside the battery [15], so the electrode structure affects the direct current internal resistance (DCIR) [16]. Therefore, studying the relationship between electrode structure and DCIR can help us design batteries with high performance.

The effect of electrode structure on the internal resistance of batteries have been studied. Donglan Zhou et al. prepared PbO_2-P and PbO_2-G anodes, revealing that the PbO_2-G anode, with its more compact surface structure, exhibits higher particle connectivity and a lower internal resistance compared to the porous PbO_2-P anode [17]. Desiree Grieβl et al. found that smaller pores in the electrode structure result in increased ion diffusion resistance [18]. Yuntao Guo et al. found that the smaller the sphericity of the active material in graphite anode, the larger the contact resistance, which is predominantly influenced by the resistivity of electrode coating and collector, as well as the contact area between them [19]. Despite these findings, these studies employed simplified structural parameters that do not accurately represent the real situation, and it still lacks a quantitative relationship between electrode structure and DCIR. The structure-activity relationship of a battery is usually explored through electrochemical modeling [20]. The classical P2D model assumes homogeneous electrode particle size, which does not accurately describe the real porous structure. Moreover, the multitude of partial differential equations adds a layer of complexity to the calculations [21,22]. The emerging pore network model (PNM) has garnered favor among researchers, which accurately extract the inhomogeneous structure of electrodes and boasts computationally efficient [23]. Currently, PNM has been successfully applied to LIB [24–26]. Studies have utilized PNM to investigate the effects of tortuosity [27], particle size distribution [27], connectivity [28], and porosity [29] on performance. The precision of determining the DCIR hinges on the judicious choice of calculation methods. Currently, the common DCIR test methods are Hybird Pulse Power Characterization (HPPC) [30] and Japan Electric Vehicle Standard (JEVS) [31]. The JEVS method uses a series of currents from 0 to 10 C, which can avoid the bias of the results generated by using a single current a limitation characteristic of the HPPC method [32]. Its demonstrated ability to provide more reliable and accurate outcomes compared to the HPPC method.

Moreover, machine learning has been widely applied to electrode design [33,34]. Yoichi Takagishi et al. used artificial neural network (ANN) to forecast the charge and discharge specific resistance of porous electrodes and optimized the process parameters to design electrodes with excellent performance [35]. Duo Yang et al. developed a Gaussian regression model to predict battery SOH using the charging curve as input [36]. Among them, Gaussian regression machine learning is appropriated for dealing with complex regression problems with high dimensionality and small samples [37].Therefore, Gaussian regression modeling and combined it with Shapley Additive exPlanations (SHAP) interpretation [38–40] can be used to compare the degree of influence of different structural parameters on DCIR. To obtain a quantitative relationship between electrode structural parameters and DCIR, more efficient methods are required. There have been studies using symbolic regression to discover analytical formulas for predicting the lifetime of LIBs with new features [41], as well as using symbolic regression to obtain performance expressions for the relevant parameters of the battery thermal model to optimize the model [42]. Therefore, a prediction formula for calculating the DCIR from the electrode structure parameters can be derived using symbolic regression.

DCIR calculation of battery constructed from PNMs with different structural parameters using JEVS. Then combined with machine learning, the optimal electrode structure can be found [43]. Therefore, this study investigates the relationship between cathode structure and DCIR using PNM combined with machine learning. Firstly, the PNM of lithium manganate cell is constructed, as shown in Fig. 1(a). And the DCIR is simulated with the JEVS method in Fig. 1(b). Subsequently, the prediction from structure to DCIR is performed by Gaussian process regression machine learning shown in Fig. 1(c). And the Shapley value is used to interpret the results of machine learning, which can obtain several structural parameters with high influence. Finally, symbolic regression machine learning based on genetic algorithm is utilized to achieve the prediction formula for DCIR derived from the structural parameters of the electrode.

2. Model and methods

2.1. Pore network model

Fig. 2 illustrates the process of constructing the PNM. Lithium manganate ($LiMn_2O_4$) and graphite (Li_xC_6) are used as cathode and anode materials, respectively. To investigate the effect of cathode parameters on the DCIR of LIB, we randomly generate the disordered structure for the cathode using the Python package *Porespy* [44] and extract the pore-throat structure using the Python package *OpenPNM* [45], as shown in Fig. 2(a). The separator and anode electrode are randomly generated by *OpenPNM* to generate a regularized structure. PNM of lithium manganate cell is constructed, which can be divided into the electrolyte phase (ELEC), active material phase (AM), and carbon binder phase (CBD), as shown in Fig. 2(b). The settings of the relevant parameters are basically consistent with the experimental settings of Chen et al. [46], as shown in Table. SI1. Due to the low computational efficiency of the complex disordered structure, the cathode structure, which determines the quantitative relationship between cathode parameters and DCIR, is a regularized structure similar to the anode depicted in Fig. 2(b).

During battery operation, diffusion and migration of Li-ions and intercalation reactions take place. The PNM can discretize the complex partial differential equations in the P2D model, referring to the work of Zohaib et al. [26] and Mehrez et al. [47] to derive the governing equations. First, it is assumed that the intercalation reaction occurs with no change in cell volume and a uniform concentration in each pore. The PNM consists of pore-throat structure, which can be calculated using the principle of resistive series connection by considering a pore-throat-pore

structure in the model as a combined conductance. In the cell charging and discharging process mainly involves diffusive conductance, ionic conductance and electrical conductance, as shown in Eq. (1).

$$\begin{aligned} G^{ed} &= \left(\frac{l_i}{A_i D_{Li^+}} + \frac{l_{ij}}{A_{ij} D_{Li^+}} + \frac{l_j}{A_j D_{Li^+}}\right)^{-1} \\ K^{e} &= \left(\frac{l_i}{A_i k_{Li^+}} + \frac{l_{ij}}{A_{ij} k_{Li^+}} + \frac{l_j}{A_j k_{Li^+}}\right)^{-1} \\ G^{sd} &= \left(\frac{l_i}{A_i D_{Li}} + \frac{l_{ij}}{A_{ij} D_{Li}} + \frac{l_j}{A_j D_{Li}}\right)^{-1} \\ K^{ohm} &= \left(\frac{l_i}{A_i \sigma_{Li}} + \frac{l_{ij}}{A_{ij} \sigma_{Li}} + \frac{l_j}{A_j \sigma_{Li}}\right)^{-1} \end{aligned} \tag{1}$$

In the ELEC, the change in lithium ions (Li-ions) concentration, which is described by the Nernst-Planck equation and the Butler-Volmer (BV) equation as shown in Eq. (2) is caused by the diffusion and migration of Li-ions and the intercalation reaction at the solid-liquid interface. And the flux of Li-ions at the interface between the electrolyte and the fluid collector is specified to be zero.

$$V_{i,elec}\left(\frac{c_{i,elec}^{t+Vt} - c_{i,elec}^{t}}{Vt}\right) = -\sum_{j=1}^{k_{elec}} G^{ed}\left(c_{i,elec}^{t} - c_{j,elec}^{t}\right) - \frac{t_+^0}{F} a j_r^t + \frac{1 - t_+^0}{F} a j_r^t \tag{2}$$

The concentration and potential difference of the Li-ions in the ELEC drive the Li-ions to migrate, causing charge to flow and generate an electric current. The potential can be calculated using a modified Ohm's law and the BV equation as shown in the following equation. No current flows at the junction between the ELEC and the collector.

$$a j_r^t = \sum_{j=1}^{k_{elec}} K^{e}\left(\left(\varphi_{i,elec}^{t} - \varphi_{j,elec}^{t}\right) - \frac{2RT_0}{F}\left(1 - t_+^0\right) ln\left(\frac{c_{i,elec}^{t}}{c_{j,elec}^{t}}\right)\right) \tag{3}$$

Fick's law and the BV equation are used to calculate the solid phase lithium concentration, which mainly consists of lithium diffusion in the AM and intercalation reactions in the ELEC with the AM and can be expressed in Eq. (4). The PNM structure of the separator is constructed by setting all its pores in the ELEC, while specifying that lithium cannot pass from the AM to the separator, and that the flux of lithium metal at the interface between the collector and the AM is also zero.

$$V_{i,AM}\left(\frac{c_{i,AM}^{t+Vt} - c_{i,AM}^{t}}{Vt}\right) = -\sum_{j=1}^{k_{AM}} G^{sd}\left(c_{i,AM}^{t} - c_{j,AM}^{t}\right) - \frac{1 - t_+^0}{F} a j_r^t \tag{4}$$

The solid phase potential is expressed using Ohm's law and the BV equation, assuming that the CBD does not react. It can be calculated using Eq. (5).

$$\begin{aligned} a j_r^t &= -\sum_{j=1}^{k_{AM}} K_{AM}^{ohm}\left(\varphi_{i,AM}^{t} - \varphi_{j,AM}^{t}\right) \\ 0 &= -\sum_{j=1}^{k_{CBD}} K_{CBD}^{ohm}\left(\varphi_{i,CBD}^{t} - \varphi_{j,CBD}^{t}\right) \end{aligned} \tag{5}$$

The electrochemical reaction occurring at the solid-liquid interface is described by the BV kinetic equation as shown in Eq. (6). The exchange current density and overpotential are expressed by Eqs. (7) and (8). Eq. (9) defines the equilibrium potential.

$$j_r^t = i_i^0\left(exp\left(\frac{\alpha_a F\eta}{RT_0}\right) - exp\left(-\frac{\alpha_c F\eta}{RT_0}\right)\right) \tag{6}$$

$$i_i^0 = \sum_{j=1}^{k_{elec}} F k^{\alpha_a+\alpha_c} c_{j,elec}^{\alpha_a}\left(c_{i,max} - c_{i,AM}\right)^{\alpha_a} c_{i,AM}^{\alpha_c} \tag{7}$$

$$\eta_i^t = \varphi_{i,AM}^{t} - \sum_{j=1}^{k_{elec}} \varphi_{j,elec}^{t} - U_i^t \tag{8}$$

$$U_i^t = f(SOC_i) \tag{9}$$

The curve of equilibrium potential versus state of charge (SOC) in Eq. (9) is shown in Figure. SI1. Meanwhile the current is conserved in the AM and the ELEC.

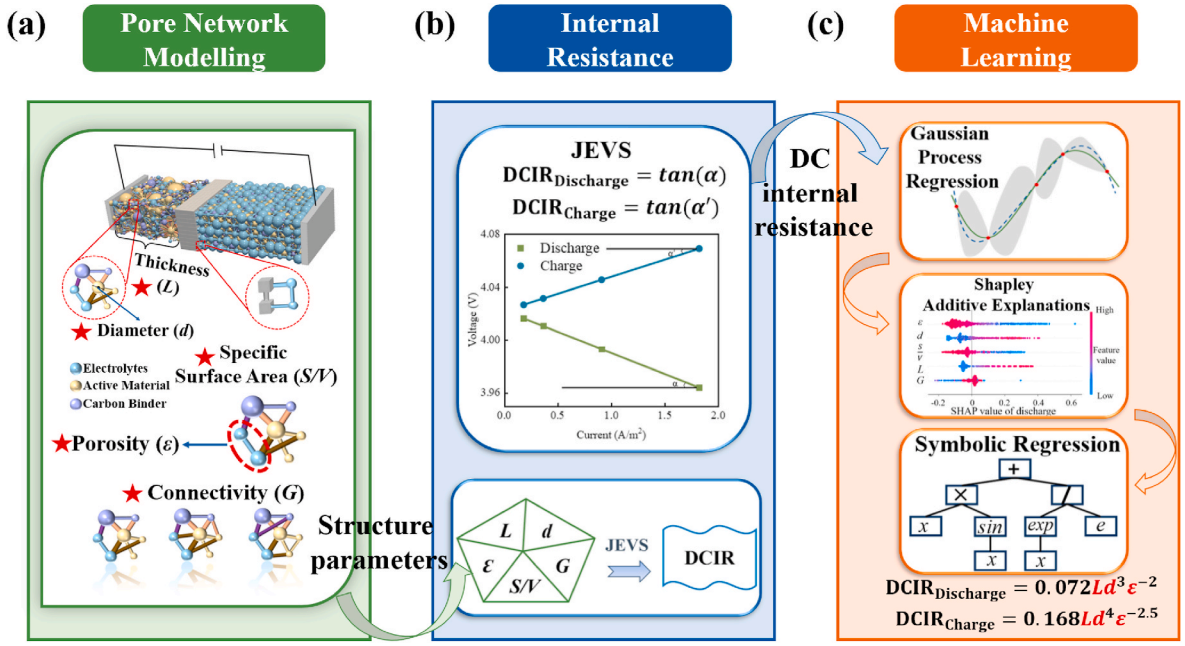

Fig. 1. Structural framework of lithium manganate cell for predicting DCIR from cathode structural parameters. **(a)** Construct PNM for lithium manganate cell with cathode characterized by specific thickness, porosity, connectivity, average particle size of active material particles, and total specific surface area of the active material particles. **(b)** The DCIR of the cell is obtained by JEVS method and the quantitative relationship between the DCIR and structural parameters is fitted. **(c)** Gaussian regression machine learning is used to predict the DCIR, and SHAP is used to interpret the machine learning results and compare the influence of the structural parameters. Finally, symbolic regression is used to derive an equation for predicting the DCIR from the structural parameters.

$$\nabla i_{elec} + \nabla i_{AM} = 0 \tag{10}$$

The interpretation of the parameters used in PNM is shown in Table 1. The settings regarding the PNM model parameters are shown in Table. SI1.

2.2. JEVS internal resistance test method

DCIR includes ohmic and polarization internal resistance, which is closely related to the capacity, power and life of the battery. It is an important parameter of the LIBs operation status. The principle for determining DCIR involves the application of a pulse current to the battery or battery pack. By leveraging Ohm's law, DCIR is calculated based on the voltage and current values taken before the battery fully polarizes. In this paper, JEVS method is used to calculate the DCIR, and the basic principle is to apply incremental pulse currents at the same SOC. As shown in Fig. 3(a), this study selects 1 C, 2 C, 5 C, and 10 C currents to charge and discharge with a pulse time of 10 s and a shelf time of 60 s [48]. As shown in Fig. 3(b), the final second of each pulse charge/discharge is selected for data collection and the voltage and current values at that time are recorded for linear fitting. The resulting slope from this analysis is the desired charging and discharging DCIR, α' and α are the slope angles of the charging and discharging voltage-current curves, as outlined in Eq. (11).

$$\begin{aligned} \mathrm{DCIR}_{\mathrm{Discharge}} &= tan(\alpha) \\ \mathrm{DCIR}_{\mathrm{Charge}} &= tan(\alpha') \end{aligned} \tag{11}$$

2.3. Machine learning

This study uses machine learning to investigate the structure-activity relationship of lithium manganate cell. In this paper, Gaussian regression machine learning, which is simple and easy to use and has high generalization ability, is used for prediction and SHAP values are used to interpret the results of machine learning [38]. The main factors affecting the DCIR are obtained, and finally the DCIR prediction formula is derived by combining symbolic regression.

Table 1
Summary of parameters used in PNM.

Nomenclature			
G^{ed}	Liquid phase diffusion conductance	j_r^t	Li-ion flux density at solid-liquid phase interface
G^{sd}	Solid phase diffusion conductance	$\varphi_{i,elec}^t$	Potential of pore i in the ELEC
K^e	Liquid phase ionic conductance	$\varphi_{j,elec}^t$	Potential of pore j in the ELEC
K^{ohm}	Solid phase electrical conductance	$c_{i,AM}^t$	Li concentration of pore i in the AM
l_i	Distance from the center of mass of pore i to the center of mass of the throat	$c_{j,AM}^t$	Li concentration of pore j in the AM
l_j	Distance from the center of mass of pore j to the center of mass of the throat	$\varphi_{i,AM}^t$	Potential of pore i in the AM
l_{ij}	Throat length	$\varphi_{j,AM}^t$	Potential of pore j in the AM
A_i	Cross-sectional area of pore i	$\varphi_{i,CBD}^t$	Potential of pore i in the CBD
A_j	Cross-sectional area of pore j	$\varphi_{j,CBD}^t$	Potential of pore j in the CBD
A_{ij}	Cross-sectional area of the throat	α_a	Anodic transfer coefficients
D_{Li^+}	Liquid phase Li-ions diffusion coefficient	α_c	Cathodic transfer coefficients
k_{Li^+}	Liquid phase Li-ions conductivity	$c_{i,max}$	Maximum Li concentration in the electrode
D_{Li}	Solid phase Li diffusion coefficient	k	Reaction rate
σ_{Li}	Solid phase Li conductivity	i_i^0	Exchange current density
$V_{i,elec}$	Volume of pore i in the ELEC	η	Overpotential
t_0^+	Li-ions liquid phase transfer coefficient	U_i^t	Equilibrium potential
$c_{i,elec}^t$	Li-ions concentration of pore i in the ELEC	i_{AM}	Current in the AM
$c_{j,elec}^t$	Li-ions concentration of pore j in the ELEC	i_{elec}	Current in the ELEC
A	Interface area between AM and ELEC		

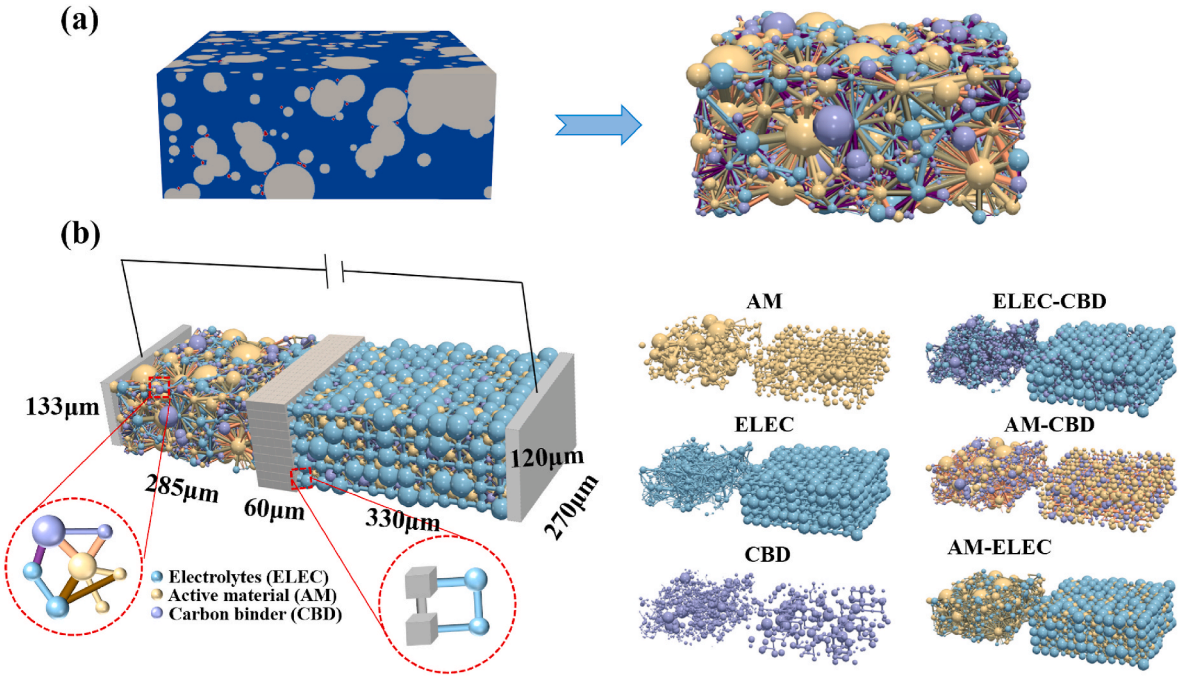

Fig. 2. **(a)** Extraction of pore-throat structure from disordered cathode structure, **(b)**PNM of lithium manganate cell.

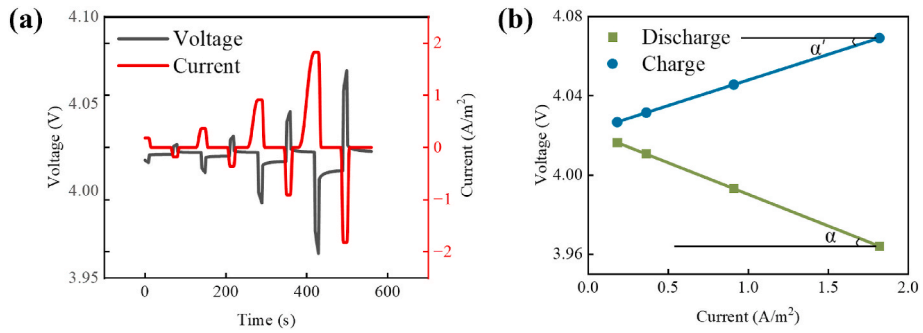

Fig. 3. **(a)** Pulse charging and discharging test with 1 C, 2 C, 5 C and 10 C, **(b)** calculation principle of JEVS internal resistance test method.

2.3.1. *Gaussian regression model and SHAP explanatory model*

A Gaussian process is a stochastic process defined over a continuous domain with infinitely many random variables obeying a Gaussian distribution and can be represented by **Eq. (12)**. Gaussian regression modeling is a nonlinear, nonparametric regression tool based on Bayesian probability theory [37].

$$f(x) \sim GP(m(x), k(x, x')) \tag{12}$$

$m(x)$ is the mean function and $k(x, x')$ is the covariance function.

The SHAP model is employed to interpret machine learning results by determining the influence of each feature on the final prediction. This method builds upon the Shapley value concept from game theory, using it to quantify the contribution of each feature within a machine learning model. The Shapley values of the features can be expressed in **Eq. (13)** [49].

$$Shapley(X_j) = \sum_{S \subseteq N \setminus \{j\}} \frac{k!(p-k-1)!}{p!} (f(S \cup \{j\}) - f(S)) \tag{13}$$

p is the total number of features, $N\setminus\{j\}$ is the set of all possible features not included, S is the set of features in $N\setminus\{j\}$, and $f(S\cup\{j\})$ and $f(S)$ denote the prediction results with and without X_j in the model, respectively.

2.3.2. *Symbolic regression model*

The specific implementation of symbolic regression is a genetic algorithm. A combination of descriptors, operators, and mathematical functions are used as chromosomes to form an individual, based on a finite fitness understanding with appropriate scoring criteria to set the basis of superiority and inferiority. Individuals with better fitness values will be copied, mated, and mutated so that solutions that better fit the objective function can effectively reproduce to the next generation, thus continuously approximating the data distribution. Genetic algorithm-based symbol regression can efficiently and automatically design hybrid descriptors that outperform single descriptors [50].

3. Results and discussion

3.1. *Pore network modeling results and validation*

The PNM of lithium manganate cell is simulated by charging with a constant current of 1C, with the voltage range set between 3.2V and 4.3V for charging and discharging cycles. Fig. 4(a) and Fig. 4(b) show the Li-ions concentration and voltage distribution diagrams of the cell at 0 and 2000 s, respectively. The concentration distribution diagrams visualize that the Li-ions pass through the separator from the cathode to the anode by diffusion and migration during the charging process. As Li-ions percolate through the anode, the concentration increases. The electrons are transferred to the anode through the external circuit, and eventually the total potential rises, which can be well confirmed by the voltage distribution diagram. The concentration and potential distribution of individual pores in different phases are shown in Figure. SI2. The simulated charging curves are compared with the experimental results of Chen et al. [46], as shown in Fig. 4(c). It can be seen that the simulated and experimental values are similar, with a larger error at 2000 s (the relative error at this point is 2 %). The later error becomes larger, this may be because, the simulation did not take into account the effect of temperature, and the experimental with the growth of charging time temperature rises, the side reaction increases, the internal resistance enlarges, resulting in the phenomenon of voltage growth rate becomes larger.

3.2. *Relationship between DCIR and structural parameters*

Fig. 5 demonstrates the quantitative relationship between the structural parameters of the cathode and the DCIR. Since these randomly generated PNM geometries may contain several different structural parameters, the main focus in describing the patterns is on the overall trends. The DCIR increases with increasing thickness (L) of the cathode electrode, as shown in Fig. 5(a) and (d). The diffusion distance of ions in the cathode material and the transport path of electrons are increased by

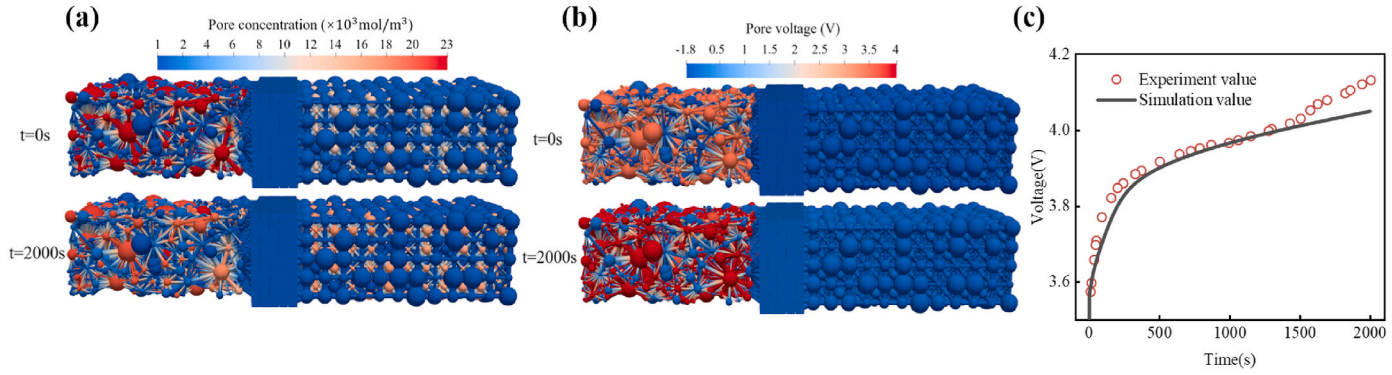

Fig. 4. **(a)** Li-ions concentration and **(b)** voltage distribution of lithium manganate cell, **(c)** PNM simulation and experimental results validation plot.

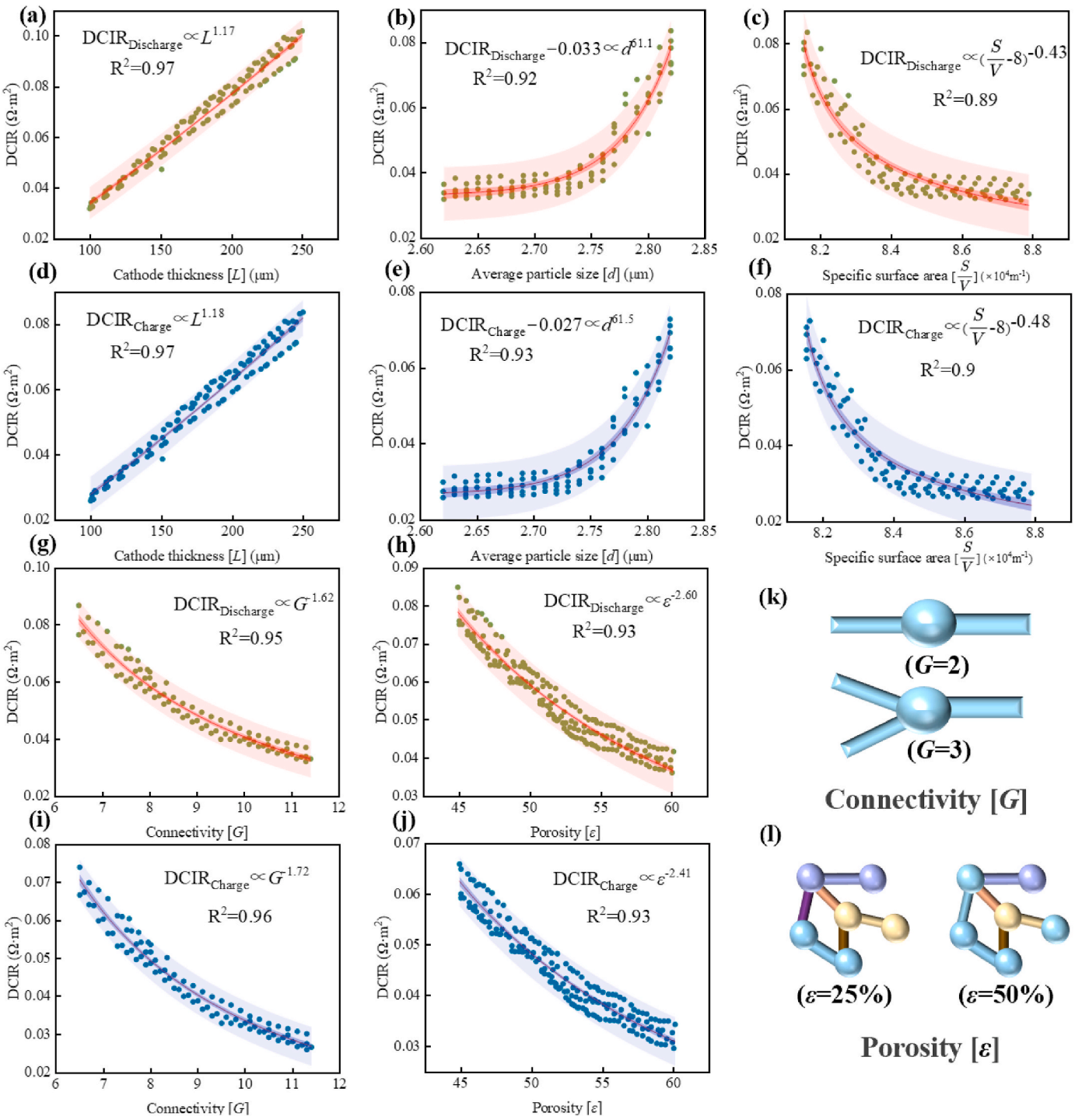

Fig. 5. Effect of electrode **(a)** L, **(b)** d, **(c)** total S/V, **(g)** G and **(h)** ε on the discharge DCIR of the cathode for lithium manganate cell; effect of electrode **(d)** L, **(e)** d, **(f)** total S/V, **(i)** G and **(j)** ε on the charging DCIR of the cathode for lithium manganate cell. Graphical representation of **(k)** G and **(l)** ε.

increasing the L of the cathode. These reasons lead to an increase in the DCIR. It is observed in Fig. 5(b) and (e) that the DCIR increases with the increase of the average particle size of the active material particles (d), which is due to the fact that decreasing the d increases the total specific surface area of the active material particles (S/V), improves the contact area between the electrolyte and the electrode material, and facilitates ionic transport, thus decreasing the DCIR, which is also demonstrated in Fig. 5(c) and (f). The DCIR in Fig. 5(g) and (i) shows a decreasing trend with increasing cathode pore connectivity (G). This is attributed to the increased G, which shortens the electron transport paths and makes the ion diffusion smoother. Fig. 5(h) and (j) demonstrate the effect of porosity (ε) on DCIR, showing a similar pattern to that of G, where an increase in ε improves the G of electron and ion transport in the cathode material and improves the contact between the AM and the ELEC, reducing the interfacial impedance. The methods of G and ε alteration are demonstrated through Fig. 5(k) and (l). The results of the charging and discharging DCIR reflect that the discharging DCIR is greater than the charging DCIR, which due to the different electrochemical reactions occurring in charging and discharging. During discharge process, Li-ions are transferred from the anode electrode to the cathode electrode, at this

time, the diffusion and migration of ions as well as the intercalation reaction occur at the cathode electrode. Due to the change of the structural parameters of the cathode electrode, the electrode structure becomes more complex, which is not conducive to the movement of ions and electrons, and therefore will increase the DCIR. Changes in the structural parameters of the electrodes can affect other properties in addition to the DCIR, e.g., when the electrode L increases, the energy density of the cell increases; when the ε is too high, the solid phase conductivity may be reduced. Therefore, where appropriate, the DCIR of the cell can be reduced and the cell performance can be improved by reducing the electrode L and d, as well as increasing the S/V, G, and ε.

3.3. Results of Gaussian regression and explained by SHAP

All the structures used to explore the relationship between structural parameters and DCIR as described previously are integrated together (a total of 487 data sets), and the dataset is normalized and divided into a training set and a test set in the ratio of 7:3. Trained for Gaussian regression machine learning in Matlab R2023b, stochastic search method is used to optimize the hyperparameters. The good prediction results can be seen in Fig. 6, where all the mean absolute errors (MAE) are less than 2 %, and the root mean square error (RMSE) of the test set of the DCIR of the discharges is a maximum of 6.14 %. These results substantiate the reliability of the model prediction using Gaussian regression machine learning.

In order to address the black-box problem of machine learning, we use the SHAP model to give possible relationships between predicted values and certain features. The deeper the red, the higher the predicted value; the bluer the color, the lower the predicted value. SHAP values reflect the impact of feature elements on the model's output. As shown in Fig. 6(c) and (f), the eigenvalue analysis of ε, shows that when the values of ε are larger, the SHAP values are predominantly negative, indicating that the ε is inversely related to the DCIR, which is similar to the law in **Section 3.2**. However, the relationship between the G and the S/V during charging and the DCIR is again different from the pattern in Section 3.2, which may be due to the structural parameters will have some interactions with each other, affecting the final results. For example, the degree of G has a certain interaction with ε, and the S/V is affected by the d. The graphs are arranged from top to bottom according to the average absolute value of the characteristics, this arrangement is the order of the degree of influence of each structural parameter on the DCIR from the largest to the smallest. Fig. 6(c) shows that ε, d and S/V have the greatest effect on discharge DCIR, while electrode L, ε and d have a greater effect on charging DCIR, which can be observed in Fig. 6 (f). And the least influential are all G.

3.4. Symbolic regression results based on genetic algorithm

The usual formula for calculating DCIR requires the battery to be charged and discharged with a certain amount of standstill time in order to derive it and cannot be obtained directly from the factory battery. It is found that the DCIR has a certain correlation with the structural parameters of the electrode through this study, therefore, we would like to predict the DCIR formula by several important structural parameters through the symbolic regression model based on genetic algorithm. The degree of influence of different structural parameters on DCIR is analyzed when performing SHAP model interpretation. Due to the large correlation between G and ε, d and S/V. Taking into consideration, we finally selected electrode L, ε and d as input parameters for symbolic regression. The DCIR in the form of **Eq. (14)** is output according to the tree structure shown in Fig. 7(a).

$$\mathrm{DCIR} = b_1 L d^{b_2} \varepsilon^{b_3} \tag{14}$$

The 487 data sets are normalized and divided into train and test sets in the ratio of 7:3 for symbolic regression learning in Matlab R2023b. The charging and discharging DCIR is predicted by symbolic regression based on genetic algorithm as shown in **Eq. (15)** and **Eq. (16)**. The optimal values of b_1, b_2 and b_3 are derived by predicting the charging and discharging DCIR through symbolic regression based on genetic algorithm as shown in **Eq. (15)** and **Eq. (16)**. The physical significance

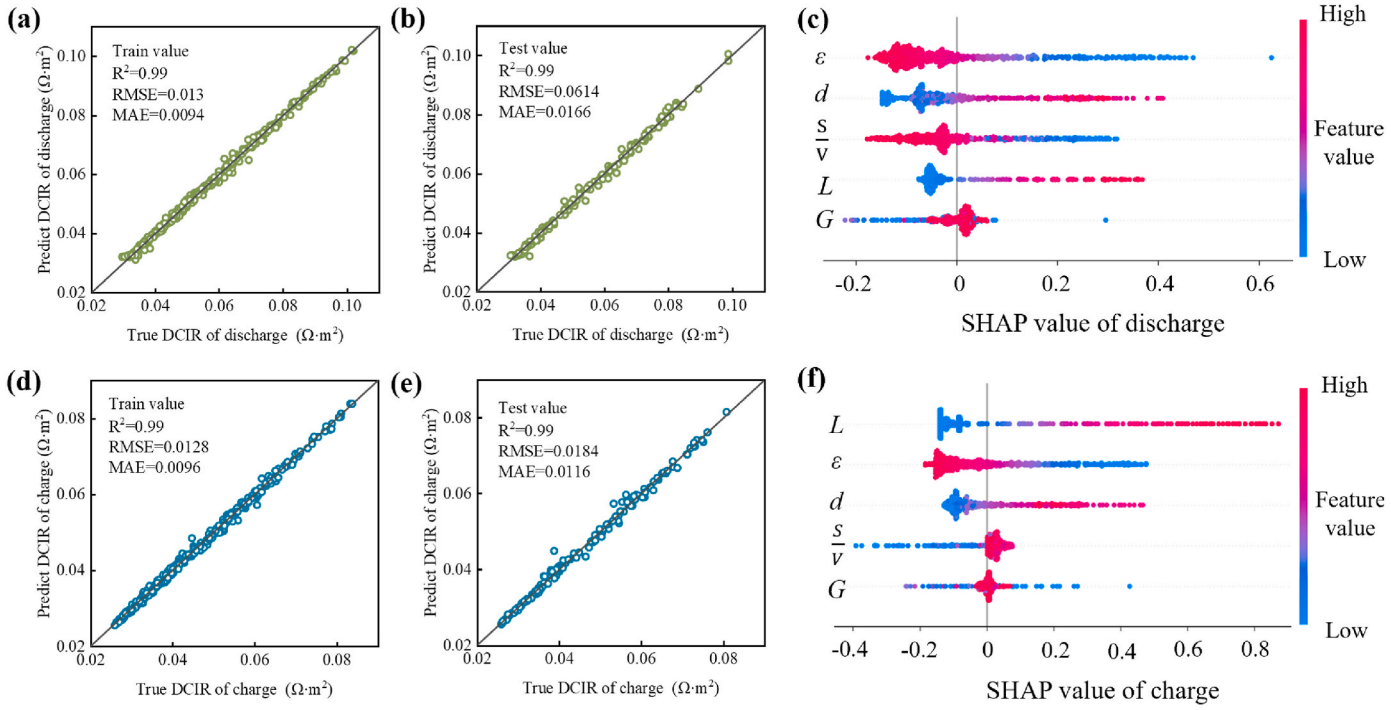

Fig. 6. Gaussian regression prediction results of lithium manganate cell discharge DCIR in **(a)** training set and **(b)** test set, **(c)** SHAP values of each structural parameter of discharge DCIR; Gaussian regression prediction results of lithium manganate cell charge DCIR in **(d)** training set and **(e)** test set, **(f)** SHAP values of each structural parameter of charge DCIR.

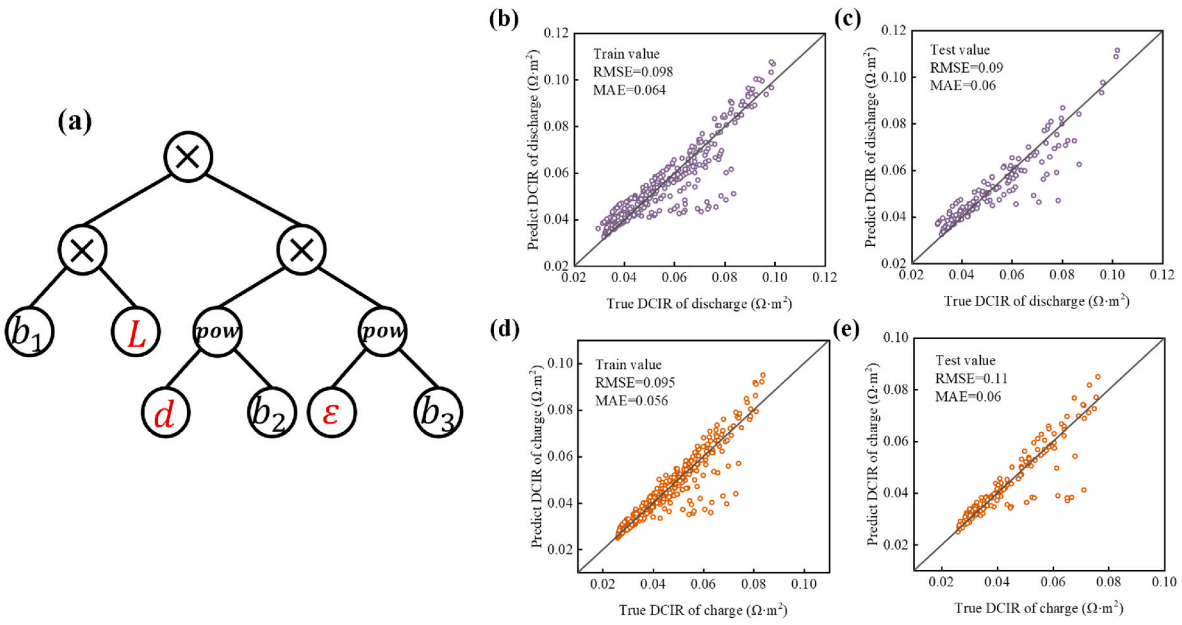

Fig. 7. **(a)** Symbolic regression to obtain the tree structure of output Eq. (14), predicted results of symbolic regression of lithium manganate cell discharge DCIR in **(b)** training set and **(c)** test set; predicted results of symbolic regression of lithium manganate cell charging DCIR in **(d)** training set and **(e)** test set.

of the coefficient b_1 in the formula for charging DCIR is 0.168 resistance per unit volume, and the physical significance of the coefficient b_1 in the formula for discharging DCIR is 0.072 resistance per unit area. The determination of these two coefficients is limited by the kinetic parameters of a specific battery. However, the process of determining this formula can help better understand the methods and factors affecting the acquisition of the battery's DCIR. Fig. 7(b–e) shows the results of the true and predicted values plotted according to the prediction formula for both the training and test sets. Both RMSE and MAE are below 20 % and 10 % respectively, which shows the accuracy of Eq. (15) and Eq. (16). Structures corresponding to scatters far from y = x may have large variations in the G or in the S/V, causing these two structural parameters to have a large impact on the DCIR.

$$\mathrm{DCIR_{Charge}} = 0.168L\frac{d^4}{\varepsilon^{2.5}} \tag{15}$$

$$\mathrm{DCIR_{Discharge}} = 0.072L\frac{d^3}{\varepsilon^2} \tag{16}$$

4. Conclusion

In this work, the relationship between various cathode structural parameters and the DCIR during charging and discharging processes are analyzed by constructing the PNM of lithium manganate cell. The results show that the DCIR is proportional to the cathode L. Although increasing the cathode L will increase the active material, it will also increase the DCIR. Therefore, a reasonable design of the cathode L can be a good balance between the energy density and the DCIR. The DCIR is negatively proportional to the cathode G. Increased the connectivity favors the movement of ions and electrons. Increasing the ε will also reduce the DCIR, however, excessively high a ε can reduce the conductivity of the solid phase. therefore, it is imperative to establish a reasonable ε value. Reducing the d can increase the S/V, thus increasing the contact area between the active material and the electrolyte in favor of the electrochemical reaction. Consequently, the DCIR increases with larger d, while a higher S/V has the opposite effect.

In order to compare the degree of influence of each structural parameter, Gaussian regression machine learning is combined and the results of the machine learning are interpreted using the SHAP model. It is found that ε, d, and S/V are the most influential factors on the discharge DCIR. In contrast, for charge DCIR, electrode L, ε, and d are identified as having a more pronounced effect. Since ε and G, d and S/V are closely related, genetic algorithm-based symbol regression is used to explore the relationship between cathode L, ε and d and charge/discharge DCIR, finally obtain $\mathrm{DCIR_{Charge}} = 0.168Ld^4/\varepsilon^{2.5}$ and $\mathrm{DCIR_{Discharge}} = 0.072Ld^3/\varepsilon^2$. This relational equation can help to improve the battery health state estimation based on the internal resistance method. The framework of combining pore network modeling and machine learning to predict the DCIR of lithium manganate cell charging and discharging established in this research fills the gap of the quantitative relationship between electrode structure and DCIR, assisting the design of lithium manganate cell cathode structure. Notably the PNM is not limited to the lithium manganate cell, most cells with porous electrodes are suitable. Meanwhile, the method to analyze DCIR with PNM and machine learning can also be applied to lead-acid batteries, fuel cells and other types of batteries, which offers theoretical insights for optimizing the microstructure of Li-ion batteries to improve their performance.

CRediT authorship contribution statement

Meiyuan Jiao: Writing – original draft, Software, Methodology. **Pan Huang:** Software, Methodology. **Zheyuan Pang:** Software. **Sijing Wang:** Software. **Honglai Liu:** Supervision. **Yiting Lin:** Writing – review & editing, Supervision, Project administration. **Cheng Lian:** Writing – review & editing, Supervision, Project administration, Funding acquisition.

Declaration of competing interest

The authors declare that they have no known competing financial interests or personal relationships that could have appeared to influence the work reported in this paper.

Acknowledgments

This work was supported by the National Natural Science Foundation of China (No. 22278127), the Fundamental Research Funds for the

Central Universities (No. 2022ZFJH004), and the Shanghai Pilot Program for Basic Research (22T01400100-18).

Appendix A. Supplementary data

Supplementary data to this article can be found online at https://doi.org/10.1016/j.jpowsour.2024.235891.

Data availability

Data will be made available on request.

References

[1] G. Zubi, R. Dufo-López, M. Carvalho, G. Pasaoglu, Renew. Sustain. Energy Rev. 89 (2018) 292–308.
[2] Y.P. Wang, A.C. Liu, Y.C. Zhu, H.L. Zhang, Y.F. Chen, S.J. Park, IEEE Trans. Power Electron. 38 (2023) 4464–4474.
[3] M. Weiss, R. Ruess, J. Kasnatscheew, Y. Levartovsky, N.R. Levy, P. Minnmann, L. Stolz, T. Waldmann, M. Wohlfahrt-Mehrens, D. Aurbach, M. Winter, Y. Ein-Eli, J. Janek, Adv. Energy Mater. 11 (2021) 37.
[4] Y.T. Lin, Y.Q. Cai, C. Lian, H.L. Liu, Chem. Eng. Sci. (2024) 295.
[5] H.G. Schweiger, O. Obeidi, O. Komesker, A. Raschke, M. Schiemann, C. Zehner, M. Gehnen, M. Keller, P. Birke, Sensors 10 (2010) 5604–5625.
[6] Y.K. Jia, P. Zhao, D.P. Finegan, J. Xu, Adv. Energy Mater. (2024) 11.
[7] W.D. Mo, Y.T. Lin, J.H. Li, C. Lian, H.L. Liu, Chem. Eng. Sci. (2024) 297.
[8] S.J. Kwon, D. Han, J.H. Choi, J.H. Lim, S.E. Lee, J. Kim, J. Electroanal. Chem. 858 (2020) 12.
[9] Y.Q. Liao, H.Y. Zhang, Y.F. Peng, Y.G. Hu, J.D. Liang, Z.L. Gong, Y.M. Wei, Y. Yang, Adv. Energy Mater. 14 (2024) 29.
[10] P.-Y. Zhang, Z.-L. Liu, J. Power Sources 195 (2010) 8013–8018.
[11] C. Qiu, G. He, W. Shi, M. Zou, C. Liu, J. Solid State Electrochem. 23 (2019) 1887–1902.
[12] K. Kuruvinashetti, H.K. Tanneru, P. Pillay, M. Packirisamy, Microsyst. Technol. (2024).
[13] A. Barai, K. Uddin, W.D. Widanage, A. McGordon, P. Jennings, Sci. Rep. 8 (2018).
[14] S. Lakshmanan, S. Annadurai, V. Sekar, R. Subban, N. Sugumaran, J. Electrochem. Soc. 168 (2021).
[15] H.L. Tao, G. Chen, C. Lian, H.L. Liu, M.O. Coppens, AIChE J. 68 (2022).
[16] T.T. Lou, W.G. Zhang, H.Y. Guo, J.S. Wang, Adv. Mater. Res. 455–456 (2012) 246–251.
[17] D. Zhou, L. Gao, Electrochim. Acta 53 (2007) 2060–2064.
[18] D. Grießl, A. Adam, K. Huber, A. Kwade, J. Electrochem. Soc. 169 (2022).
[19] Y. Guo, X. Li, Q. Qin, Z. Wang, H. Guo, J. Wang, G. Yan, J. Power Sources 569 (2023).
[20] Y.T. Lin, C. Lian, M.U. Berrueta, H.L. Liu, R. van Roij, Phys. Rev. Lett. 128 (2022).
[21] D. Marc, N. John, Electrochim. Acta 40 (1995) 6.
[22] F.F. Thomas, D. Marc, N. John, J. Electrochem. Soc. 141 (1994).
[23] P. Huang, H.L. Tao, H.L. Liu, C. Lian, AIChE J. 70 (2024) 11.
[24] G.H. Ye, W.W. Tong, X.L. Liu, X.K. Song, J.H. Zhou, X.G. Zhou, Chem. Eng. Res. Des. 149 (2019) 226–234.
[25] Z.A. Khan, P.A.G. Salaberri, T.M.M. Heenan, R. Jervis, P.R. Shearing, D. Brett, A. Elkamel, J.T. Gostick, J. Electrochem. Soc. 167 (2020) 12.
[26] Z.A. Khan, M. Agnaou, M.A. Sadeghi, A. Elkamel, J.T. Gostick, J. Electrochem. Soc. 168 (2021) 12.
[27] N. Misaghian, M.A. Sadeghi, E. Roberts, J. Gostick, J. Electrochem. Soc. 169 (2022) 16.
[28] A. Torayev, A. Rucci, P. Magusin, A. Demortière, V. De Andrade, C.P. Grey, C. Merlet, A.A. Franco, J. Phys. Chem. Lett. 9 (2018) 791–797.
[29] M.A. Sadeghi, M. Aganou, M. Kok, M. Aghighi, G. Merle, J. Barralet, J. Gostick, J. Electrochem. Soc. 166 (2019) A2121–A2130.
[30] Idaho National Engineering &Environmental Laboratory (INEEL). Freedom CAR Battery Test Manual for Power-Assist Hybrid Electric Vehicles.DOE/ID-11069, 2003. PDF version.
[31] Japan electric vehicle society. Test method of input and out put power density of nickel-hydride battery for Hybrid Electric vehicles[S], 2003. Japan.
[32] X.F. Shen, B.X. Sun, H.F. Qi, X.B. Shen, X.J. Su, in: Applied Energy Symposium and Forum - Low-Carbon Cities and Urban Energy Systems (CUE), Elsevier Science Bv, Shanghai, PEOPLES R CHINA, 2018, pp. 550–555.
[33] H.Y. Xu, J.E. Zhu, D.P. Finegan, H.B. Zhao, X.K. Lu, W. Li, N. Hoffman, A. Bertei, P. Shearing, M.Z. Bazant, Adv. Energy Mater. 11 (2021) 34.
[34] H. Tao, S. Wang, H. Liu, C. Lian, Angew. Chem. (2024) e202418447.
[35] Y. Takagishi, T. Yamanaka, T. Yamaue, Batteries 5 (2019).
[36] D. Yang, X. Zhang, R. Pan, Y. Wang, Z. Chen, J. Power Sources 384 (2018) 387–395.
[37] F. Berns, J. Huwel, C. Beecks, SN computer science 3 (2022) 300.
[38] Z.Y. Pang, P. Huang, C. Lian, C. Peng, X.C. Fang, H.L. Liu, Chem. Eng. Sci. 283 (2024) 10.
[39] K. Aas, M. Jullum, A. Loland, Artif. Intell. 298 (2021) 24.
[40] W.Z. Tawfik, S.N. Mohammad, K.H. Rahouma, E. Tammam, G.M. Salama, J. Energy Storage (2023) 73.
[41] J. Xiong, T.-X. Lei, D.-M. Fu, J.-W. Wu, T.-Y. Zhang, Prog. Nat. Sci.: Mater. Int. 32 (2022) 793–799.
[42] R.I. De la Sotta, P.A. Estévez, J.R. Vergara, W.R. Calderón-Muñoz, J. Energy Storage 73 (2023).
[43] X. Fu, Y. Zhou, J. Huang, L. Feng, P. Yu, Q. Zhang, W. Yang, Y. Wang, Adv. Energy Mater. (2023) 13.
[44] J. Gostick, Z. Khan, T. Tranter, M. Kok, M. Agnaou, M. Sadeghi, R. Jervis, J. Open Source Softw. 4 (2019).
[45] A.M. Gostick J, J. Hinebaugh, T. Tranter, M.A. Hoeh, H. Day, B. Spellacy, M. H. Sharqawy, A. Bazylak, A. Burns, W. Lehnert, Comput. Sci. Eng. 18 (2016) 60–74.
[46] J.W. Chen, E. Jiaqiang, S.Y. Kang, X.H. Zhao, H. Zhu, Y.W. Deng, Q.G. Peng, Z. Q. Zhang, Energy 187 (2019) 14.
[47] M. Agnaou, M.A. Sadeghi, T.G. Tranter, J.T. Gostick, Comput. Geosci. 140 (2020) 12.
[48] B.S. Xiaofeng Shen, Hongfeng Qi, Xiaobo Shen, XIaojia Su, Energy Proc. 152 (2018) 550–555.
[49] Z.Q. Li, Comput. Environ. Urban Syst. 96 (2022) 18.
[50] Z. Pan, Y.G. Zhou, L. Zhang, ACS Appl. Mater. Interfaces 14 (2022) 11.